DEFINING PUPIL KNOWLEDGE REQUIREMENTS FOR ROMAN SPACE TELESCOPE INTEGRATED PAYLOAD ASSEMBLY TESTING

A Thesis

Presented to the Faculty of the Graduate School

of Cornell University

in Partial Fulfillment of the Requirements for the Degree of

Masters of Science in Aerospace Engineering

by

Kaitlyn Chandler Summey

December 2022

This document is for the public domain.

ABSTRACT

This thesis examines the use of phase retrieval to characterize an optical system under testing conditions with pupil knowledge error. The purpose of this research is to define pupil knowledge requirements for the integrated payload testing of the Roman Space Telescope (RST). I have conducted a Monte Carlo study to determine how uncertainty in the location of the ground support equipment relative to the payload will affect the ability to use image-based wavefront sensing during the test to characterize system alignment. This test will be conducted in the Space Environment Simulator (SES) with the presence of Wavefront Error (WFE) due to gravity sag on the primary mirror. In this study, I incrementally decentered a piece of ground support equipment, the SubAperture Metrology System (SAMS), and evaluated how the phase retrieval algorithm attempted to fit the wavefront with the pupil mismatch. The results of this study are a factor in the overall Integrated Payload Assembly (IPA) testing WFE budget.

BIOGRAPHICAL SKETCH

Kaitlyn Summey graduated from the University of Georgia with a degree in Computer Systems Engineering in 2019. During her time at the University of Georgia, she participated in undergraduate research in the Kner Lab as an undergraduate research assistant and in the Small Satellite Research Laboratory as the Payload Lead for the Spectral Ocean Color small satellite. She began working at NASA in 2016 as an intern at Armstrong Flight Research Center before transitioning to a Pathways student trainee at Goddard Space Flight Center. Following her bachelor's degree, she entered graduate school at Cornell University in the Mechanical and Aerospace Engineering Department and joined the Space Imaging and Optical Systems Lab.

This is dedicated to my role model and grandfather, Randy Turner.

ACKNOWLEDGEMENTS

First, I must acknowledge that the NASA Pathways program made this work possible. As a member of the Roman Space Telescope wavefront sensing and control team, I conducted a portion of this work as a part of my regular duties. This project was not externally or competitively funded.

On a more personal note, I would like to thank my advisor, Professor Dmitry Savransky. I would not be where I am today without his support and mentorship over the last few years. I am also grateful for my labmates in the Space Imaging and Optical Systems Laboratory who were always quick to lend a helping hand or provide comedic relief.

I would also like to thank the NASA Goddard Space Flight Center wavefront sensing and control team. Specifically, my group lead Bruce Dean, for taking the risk and bringing an undergraduate computer engineering major into an optics group, my mentors on the RST engineering team, Matt Bolcar, Alden Jurling, and Matt Bergkoetter, for patiently supporting me through the learning curve that followed, and the JWST wavefront sensing and control team for giving me the opportunity to work on the mission that inspired me to pursue a career in optics.

My time in the Small Satellite Research Laboratory at the University of Georgia played a large role in my decision to go to graduate school. My mentor, David Cotten, and his enthusiastic encouragement, made me more confident in myself as an engineer and researcher. This lab, and the students who worked in it, made an incredible impact in my professional and personal life, and I feel lucky to have been a part of it.

Finally, I want to thank my family and my partner for always being there to support me.

TABLE OF CONTENTS

Biographical Sketch . . . iii
Dedication . . . iv
Acknowledgements . . . v
Table of Contents . . . vi
List of Figures . . . vii

1 INTRODUCTION 1
1.1 Background . . . 1
1.1.1 Nancy Grace Roman Space Telescope . . . 1
1.1.2 Fourier Optics . . . 3
1.1.3 Integration and Testing . . . 8
1.2 Purpose . . . 13

2 METHODS 15
2.1 Focus Diverse Phase Retrieval . . . 15
2.2 Simulations . . . 21

3 RESULTS 26
3.1 Roman Space Telescope IPA Test Simulations . . . 26
3.1.1 Ideal Model . . . 26
3.1.2 Monte Carlo Perturbed Models . . . 30
3.1.3 Gravity Sag Model . . . 31

4 CONCLUSION 37

Bibliography 39

ACRONYMS

CGI Coronagraph Instrument.

FPA Focal Plane Array.

HST Hubble Space Telescope.

IPA Integrated Payload Assembly.

JWST James Webb Space Telescope.

NASA National Aeronautics and Space Administration.

OLAFS Optical Large Aperture Flat System.

RMS Root Mean Squared.

RST Roman Space Telescope.

SAMS SubAperture Metrology System.

SES Space Environment Simulator.

WFE Wavefront Error.

WFI Wide-Field Instrument.

LIST OF FIGURES

1.1 Integrated Payload Assembly 1
1.2 Euler's formula 4
1.3 Wavefront shown in ray diagram 5
1.4 Illumination of an aperture by a point source 5
1.5 Propagation of a point source 6
1.6 IPA test configuration 10
1.7 Beam path during IPA testing 11
1.8 Illustration of beam position on focal plane array 12
1.9 Illustration of decentering effects on pupil geometry 14

2.1 Flow diagram of phase retrieval algorithm 20
2.2 Flow diagram of Monte Carlo study 22
2.3 Model initial pupil reference 25

3.1 Double pass results for ideal model 27
3.2 Comparison of results across multiple fiber locations 28
3.3 FPA sweep for ideal model 29
3.4 FPA sweep statistics for ideal model 30
3.5 Results for 30 perturbed models 32
3.6 Double pass results for gravity model 33
3.7 FPA sweep for gravity model 34
3.8 FPA sweep statistics for gravity model 35
3.9 Pupil clipping effects 36

CHAPTER 1

INTRODUCTION

1.1 Background

1.1.1 Nancy Grace Roman Space Telescope

The Nancy G. Roman Space Telescope (RST), NASA's next flagship observatory, will provide insight into multiple areas of astrophysics including universal expansion, dark energy, and exoplanets. The two instruments on-board are the Wide-Field Instrument (WFI) and the Coronagraph Instrument (CGI). The WFI

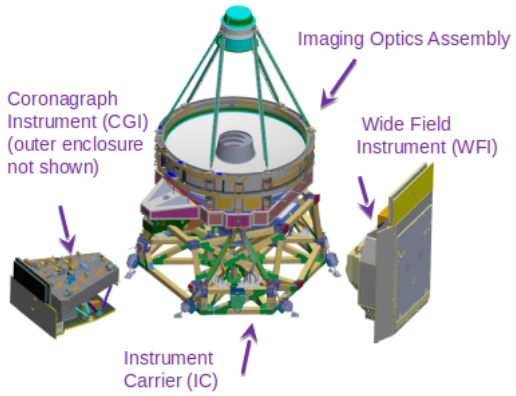


Figure 1.1: The integrated payload assembly (IPA) consists of the imaging optics, wide-field instrument (WFI), the coronagraph instrument (CGI), and the instrument carrier [3]

is an infrared imager designed to have a very large field of view, which will enable the instrument to capture data at a rate 500 times that of its predecessor, the Hubble Space Telescope (HST). While the size of the primary mirror is the same as in HST, this observatory's field of view will be 100 times that of HST's infrared instrument.

The CGI will study exoplanets by blocking out the light from distant stars. This instrument will be the most powerful coronagraph ever flown due to the active wavefront control capabilities. RST is projected to discover ∼2,600 exoplanets over its five year mission timeline [4].

HST taught the world the importance of extensive ground verification with its mirror defect [14], and the James Webb Space Telescope (JWST) proved that impeccable engineering and stringent testing yields beautiful results [8, 16, 15]. The lessons learned from these two great observatories will be carried throughout the integration and testing of the RST which, like JWST, will be at the second Earth-Sun Lagrange point—an unserviceable orbit.

These missions used an image-based wavefront sensing technique, phase retrieval, for on-sky verification. This technique characterized the HST mirror flaw [8], and most recently, played an integral part in the alignment of the JWST.

Throughout testing and on-sky alignment JWST proved that phase retrieval is a novel method of wavefront sensing that can be used to characterize the performance from the individual components to the integrated payload [15, 5]. The Roman wavefront sensing and control team has outlined a testing plan that includes a new applications of this well-established image based wavefront sensing technique [6]. With previous observatories, the main contribution of phase retrieval began after launch. However, the RST will require a new approach to pre-launch verification that involves using phase retrieval as a primary method of wavefront sensing during final integration and testing.

1.1.2 Fourier Optics

The goal of optical testing can be simplified to the following premise: trying to understand how light changes as it interacts with a medium/component/system. Many factors can influence this interaction, including system misalignment, stray light, and environmental effects (vibration, temperature). The measurement of this interaction (or wavefront) characterizes the component or system performance and offers insight into which factors may be affecting the performance. Phase retrieval [9, 6] is a method of wavefront sensing that uses knowledge of the optical system and imaged data to characterize how the light changes as it propagates through an optical system. This method requires minimal specialized equipment and can be used to characterize a system from the component level to final integration. Phase retrieval uses fundamental concepts in Fourier optics to relate light coming into the system with a point of light that is focused onto the detector (or the point spread function).

Wave Equations and Euler's Formula

Light is a wave modeled by a periodic function with amplitude A and traveling through space with velocity c at time t. The phase, φ, is the angle of a wave at a fraction of the period, T, visualized in Figure 1.2. Represented using Euler's Formula, a wave $u(P,t)$ defined by position, P, and time,t, is

$$u(P,t) = A(P)\cos(2\pi vt + \varphi(P) = \Re\{U(P)e^{-j2\pi ct}\}\,. \tag{1.1}$$

The relationship between the phase and wavefront can be visualized using geometric optics, shown in Figure 1.3, where light is represented as a ray traveling through space that bends or changes direction as it encounters surfaces such as a

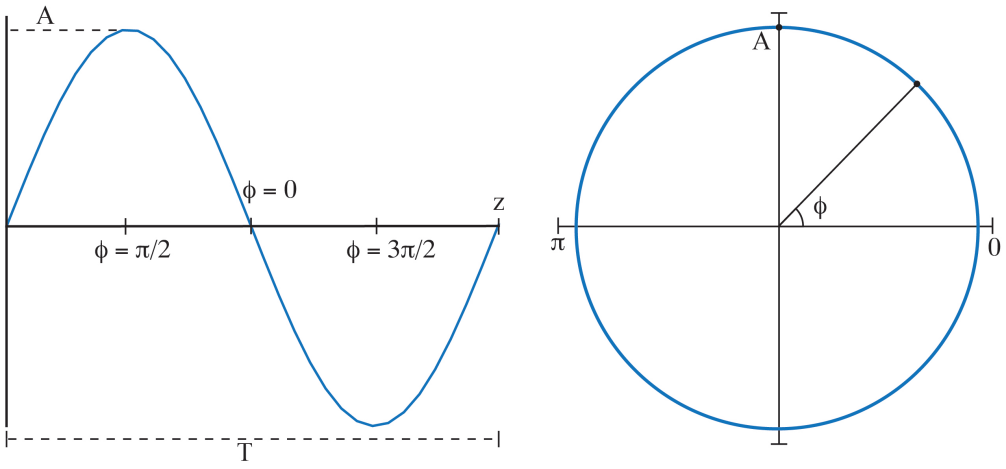


Figure 1.2: Visualization of the phase of a periodic function defined by Euler's formula.

lens or mirror. Ray diagrams are a useful way to show how light travels through a system in two dimensions. The wavefront is a point of constant phase across multiple rays of light. In the two dimensional representation, the dotted line perpendicular to the direction in which the light ray is traveling denotes the wavefront. The simple system below shows collimated light being focused by a lens. Since the wavefront is perpendicular to the rays of light, we see the wavefront change with the angle of the rays after passing through the lens in Figure 1.3.

Transitioning to modeling light as waves diverging from a point source traveling through space as shown in Figure 1.4, the disturbance of a point source from P_2 at the point on a screen P_1 is given by

$$U(P_1) = \frac{Ae^{jkr_{21}}}{r_{21}}. \tag{1.2}$$

Since the time-dependence of the field is harmonic, the time dependent variables are replaced with the wave number k, defined by the wavelength, and the vector from P_2 to P_1, r_{21}. The sign of the exponential indicates that the wave is diverging from P_2, meaning that the waves emitted earlier are traveling away

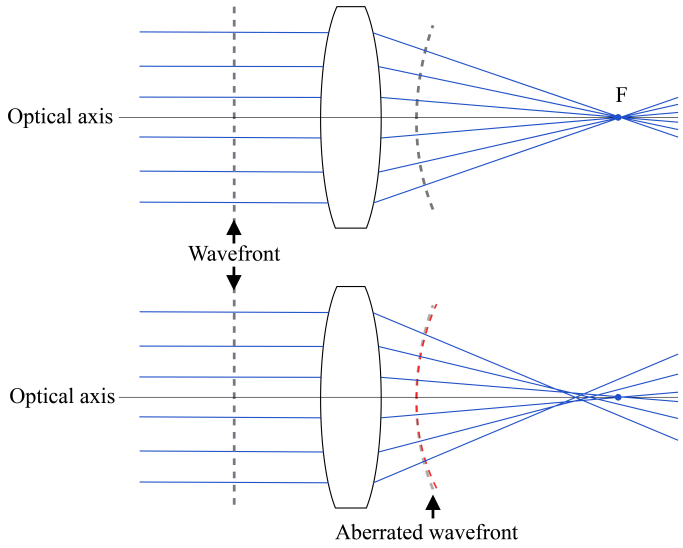


Figure 1.3: Simple ray diagram with wavefront shown as dotted grey line illustrating how wavefront aberrations affect image formation

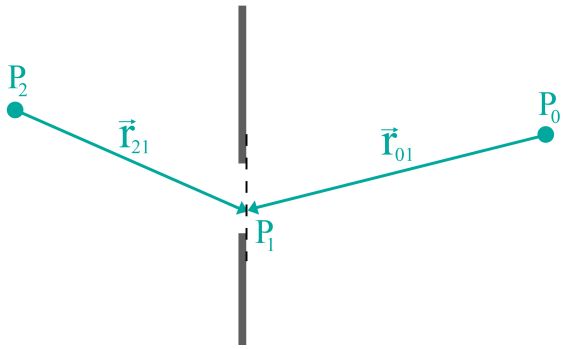


Figure 1.4: Illumination of an aperture by a point source

from the point source.

Fresnel Propagation

The Huygens-Fresnel principle provides a means to the complex field disturbance of a point source $U(P_0)$ in an enclosed space Σ at P_1 shown in Figure 1.5.

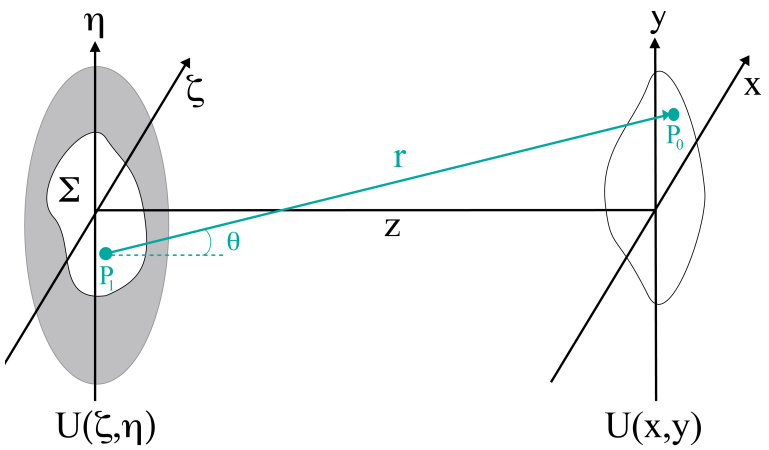


Figure 1.5: The propagation of a point source within an enclosed area Σ from a point P_1 in the input field to a point P_0 in the output field

This is defined as

$$U(P_0) = \frac{1}{j\lambda} \iint_{\Sigma} U(P_1) \frac{e^{jkr}}{r} \cos\theta ds \tag{1.3}$$

where $U(P_1)$ is the field disturbance at P_1, λ is wavelength, k is the wave number, and Σ is the enclosed space around P_0. Plugging in the value of

$$\cos\theta = \frac{z}{r}, \tag{1.4}$$

we get [13]

$$U(P_0) = \frac{1}{j\lambda z} \iint_{\Sigma} U(P_1) \frac{e^{jkr}}{r^2} ds. \tag{1.5}$$

Going forward, we will look at the disturbance in terms of the planes $U(\xi, \eta)$ and $U(x, y)$, or the pupil and image plane respectively. In an optical system, the pupil plane represents a point where the light is limited by a component–like an aperture, and the image plane is where an image is formed. Point sources of light traveling through an aperture produces spherical waves that interact with one another as they travel through space. We will show that the propagation of light from the pupil plane to the image plane can be achieved with a Fourier transform.

Expanding the Fresnel principle to show the disturbance of the input field

$U(\xi, \eta)$ on $U(x, y)$ we have

$$U(x,y) = \iint_{-\infty}^{\infty} U(\xi,\eta)\frac{e^{jkr}}{r}\frac{z}{j\lambda r}d\xi d\eta \tag{1.6}$$

Using the distance formula to calculate r yields

$$r = \sqrt{z^2 + (x-\xi)^2 + (y-\eta)^2}. \tag{1.7}$$

Fresnel's approximation uses the binomial expansion of square to rewrite this equation in a more usable form [13]

$$r \cong z + \frac{(x-\xi)^2 + (y-\eta)^2}{2z}. \tag{1.8}$$

Now, r is a defined using the coordinate systems of the pupil and image plane. Plugging this back into 1.1.2 and simplifying,

$$U(x,y) = \frac{e^{jkz}}{j\lambda z}e^{\frac{jk}{2z}(x^2+y^2)}\iint_{-\infty}^{\infty} U(\xi,\eta)e^{\frac{jk}{2z}(\xi^2+\eta^2)}e^{\frac{-jk}{z}(x\xi+y\eta)}. \tag{1.9}$$

The quadratic phase term $U(\xi,\eta)e^{\frac{jk}{2z}(\xi^2+\eta^2)}$ is cancelled out when a lens focuses light at the image plane as stated in Fraunhoffer's approximation. Dropping the quadratic phase term yields

$$U(x,y) = \frac{e^{jkz}e^{j\frac{k}{2z}(x^2+y^2)}}{j\lambda z}\iint_{-\infty}^{\infty} U(\xi,\eta)e^{\frac{-jk}{z}(x\xi+y\eta)}d\xi d\eta. \tag{1.10}$$

The equation above, neglecting $\frac{e^{jkz}e^{j\frac{k}{2z}(x^2+y^2)}}{j\lambda z}$, which is constant with respect to each point in the image plane, shows that the propagation of light from the pupil plane to the image plane is the Fourier transform of the pupil function.

The electric field at the image plane can then be used to calculate the intensity or point spread function. In cases where finding the intensity distribution at the focal plane is the desired measurement, the quadratic term preceding the integral is of no consequence and is dropped from the calculation. This

field propagation is the foundation of phase retrieval and provides a mathematical background for the relationship between the pupil function and the point spread function. [13]

1.1.3 Integration and Testing

RST will undergo extensive testing at every step of integration. The final payload verification will take place in the Space Environment Simulator (SES) at NASA's Goddard Space Flight Center following the integration of the science instruments to the instrument carrier and the optical telescope assembly.

Leading up to final integration, there will be component and subsystem level testing to ensure the instruments are performing as expected, and the final stage in integration testing will focus on verifying the alignment of the instruments with the telescope assembly. Throughout integration and testing, a variety of procedures will be used to characterize the system, and in many cases multiple wavefront sensing methods will be used to cross check results [2]. Prior to instrument integration, the image formation assembly testing will use phase retrieval and interferometry simultaneously in order to verify that the results from both methods are consistent. JWST provided a successful demonstration of phase retrieval in testing environments, however, it also showed the value of using secondary verification whenever possible.

In order to verify the functionality of a space telescope on the ground, the instruments must be tested in an environment that is comparable to what they will experience on orbit. The temperature and pressure in the space environment can be approximated in a thermal vacuum chamber, but there are some com-

plications that cannot be avoided. At the payload integration stage, RST will no longer be compatible with the gravity off-loaders that support the weight of the primary mirror. The gravity sag of the primary mirror presents a unique engineering problem: how can we verify the alignment of the telescope in the presence of inherent, significant wavefront error?

Integrated Payload Testing

The Integrated Payload Assembly (IPA) consists of the optical telescope assembly along with the two instruments. This study is focused on the WFI. The payload will be tested in a pseudo-double pass configuration in the SES. To achieve a double-pass configuration, there are two important pieces of ground support equipment required for this test. The first is the 1.8 m Optical Large Aperture Flat System (OLAFS) that is mounted on a tip/tilt stage to the dome of the testing chamber. Second is the SubAperture Metrology System (SAMS)– an off-center subaperture mounted to the payload shroud. The SAMS limits the size of the beam to 1.5 m. These components are offset to align with the WFI channel. As shown in Figure 1.7, the beam of light will originate from one of the eight fiber sources adjacent to the Focal Plane Array (FPA) detector of the WFI. The light will travel through the WFI and optical telescope assembly in reverse, forming a collimated beam reflecting off of the primary mirror.

This collimated beam is then clipped by the off-center SAMS and reflected from the OLAFS. The beam then travels back through the telescope to be imaged by the fFPA detector. By using combinations of the eight fibers and the tip-tilt capabilities of the OLAFS, the entire WFI field of view can be sampled. The FPA consists of an array of eighteen 4k X 4k detectors mounted to a hexapod.

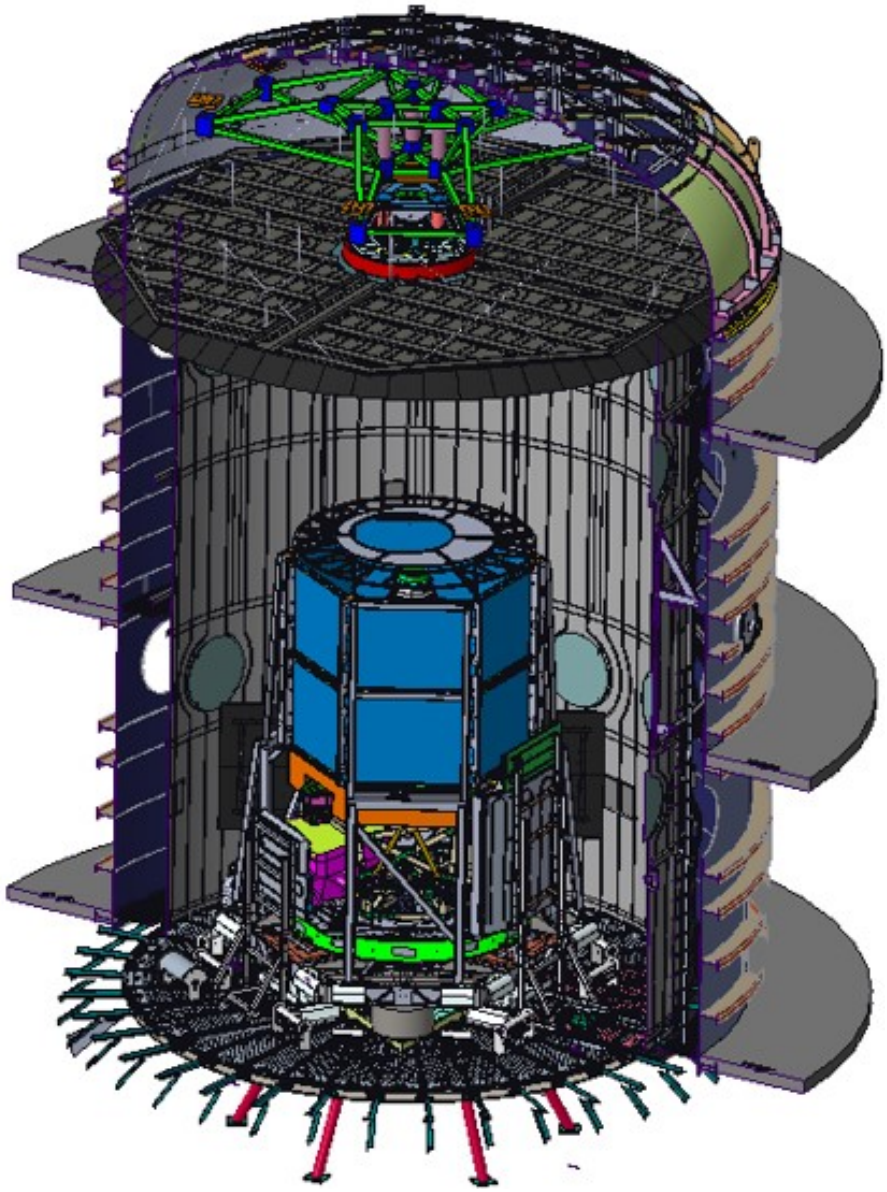


Figure 1.6: The IPA in the SES chamber with the SAMS mounted to the payload shroud and the OLAFS mounted to the dome of the testing chamber. [2]

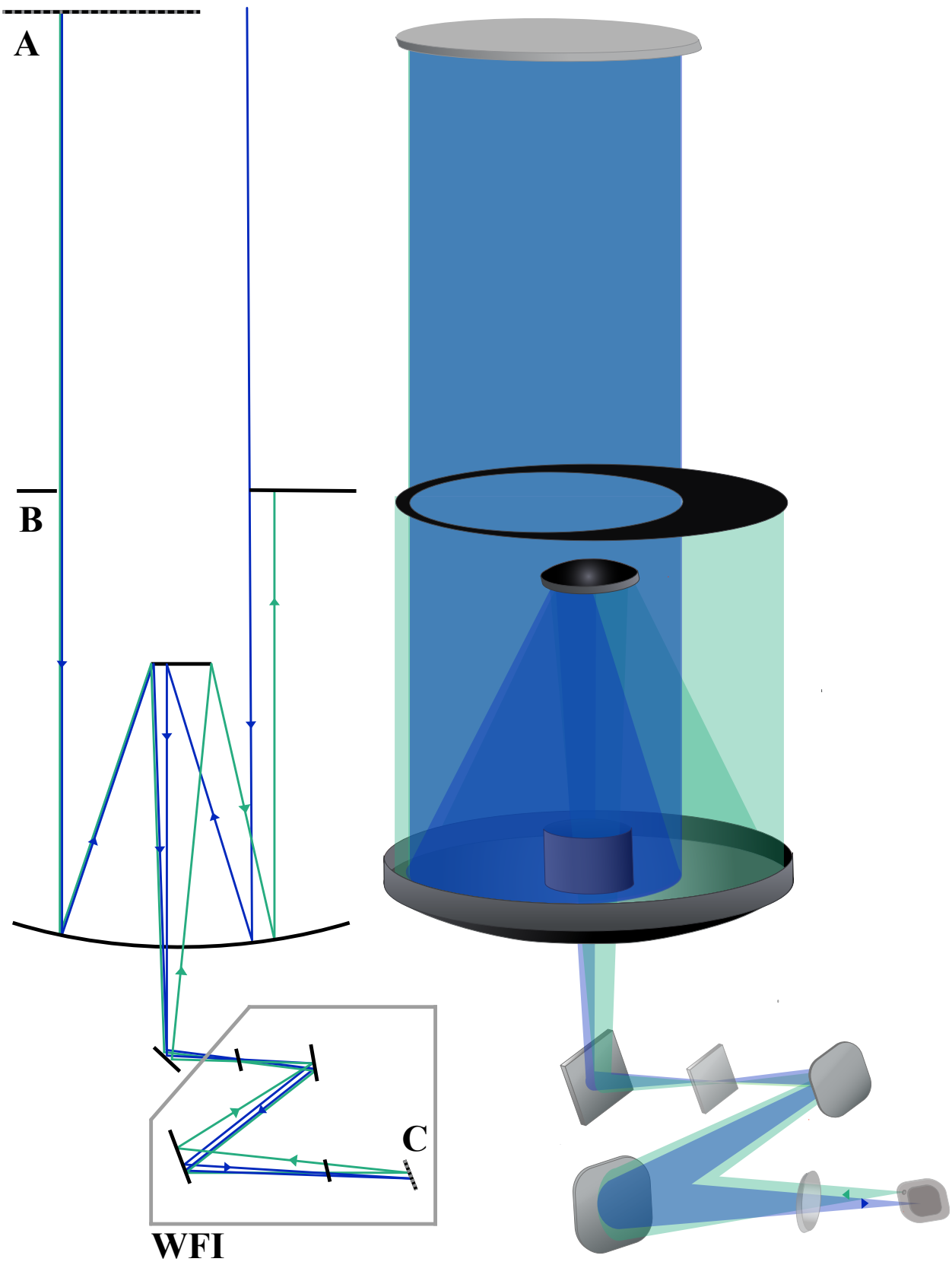


Figure 1.7: The beam path for the IPA test setup showing the OLAFS (A), SAMS (B), and the FPA (C). The moving components are indicated with the dotted line.

An example field pass can be seen in Figure 1.8. Fibers E-H will be illuminated simultaneously, and the OLAFS will be tilted to six different positions to translate the beams across the FPA detectors[1]. During this test, the FPA will be

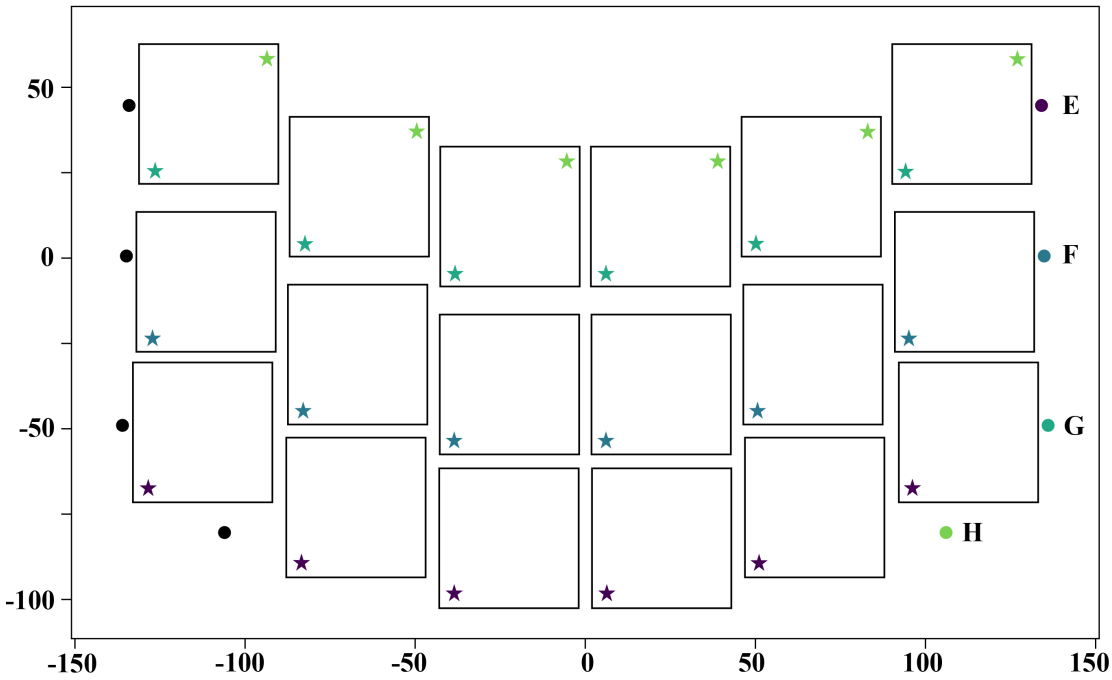


Figure 1.8: An example of a test sweep using the four fibers on the right side of the FPA. The fibers wil be translated from left to right by six tilts of the OLAFS.

translated through focus by the alignment compensation mechanism to three different positions for focus diversity. In order to minimize the use of the FPA hexapod in 1-g, the FPA will be translated to a focus position, and then data will be collected for every field point at that position before moving on to the next focus position.

Since the OLAFS and SAMS are undersized compared to the primary mirror, these components will need to be aligned with the telescope in order to conduct this test. Considering the component alignment and presence of gravtiy sag, the IPA test presents many unique challenges that need to be understood be-

fore testing plans can be finalized. This study will use optical models[10] to confirm that image-based wavefront sensing can be used to overcome the challenges related to gravity sag, and it will provide a better understanding of how phase retrieval performs with the combination of gravity sag and the additional ground support equipment required for this test[2].

1.2 Purpose

Phase retrieval is conventionally dependent on a well-defined pupil function, but in a lab or testing environment, especially those with extreme environmental changes, precise alignment of optical assemblies with external support equipment is not always feasible, introducing pupil knowledge error. The purpose of this investigation is two-fold. From a broad perspective, we want to understand how phase retrieval performs during this test with inherent, uncorrected pupil knowledge error. Based on the broader investigation, we intend to define testing requirements and alignment knowledge tolerances for RST final verification.

As the telescope cools to operating temperatures in the testing chamber, there are expected temperature deformations in the ground support equipment that will decenter these components in the system pupil function. The effects of decentering on the SAMS and OLAFS is shown in Figure 1.9. The SAMS will determine the location of the secondary mirror and supporting struts in pupil function, and OLAFS decentering will result in clipping of the edges of the pupil function.

This study is intended to determine how precisely we need to know the lo-

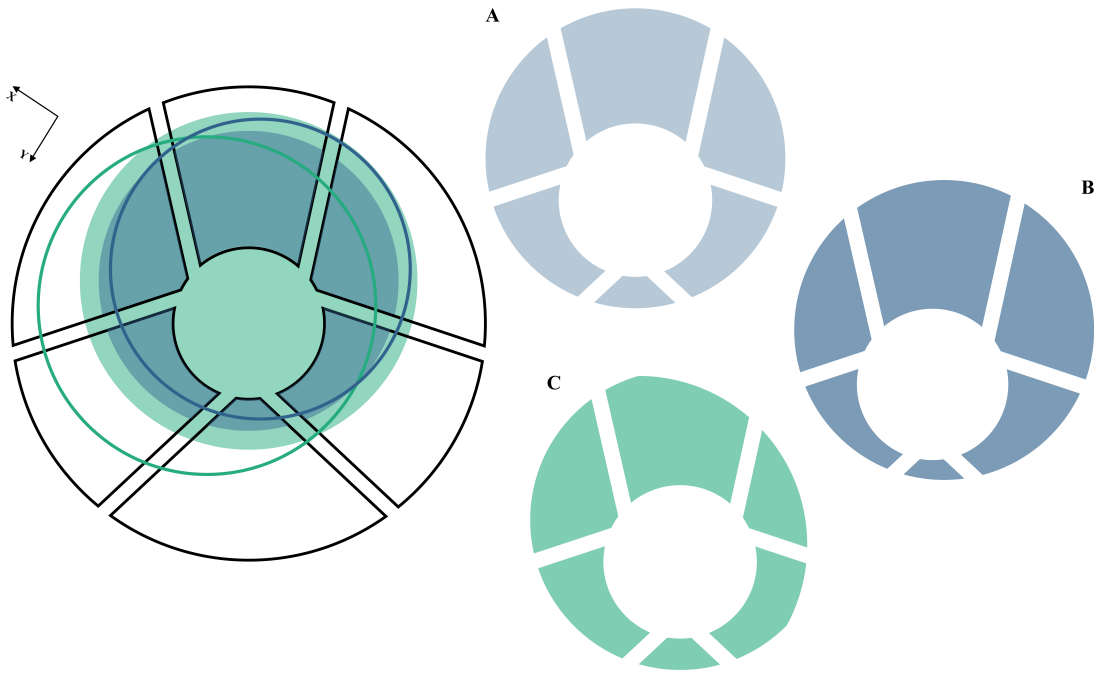


Figure 1.9: Effects of decentering on the pupil geometry for SAMS and OLAFS. The SAMS and OLAFS are shown as an overlay on the full primary mirror with rings representing exaggerated misalignment scenarios. In (A) the components are aligned. (B) shows that SAMS decentering changes the secondary mirror and strut location in the pupil while (C) indicates that OLAFS decentering results in clipping along the edges of the pupil.

cation of the SAMS relative to the IPA.

CHAPTER 2

METHODS

2.1 Focus Diverse Phase Retrieval

Phase retrieval is an image-based wavefront sensing technique that uses Fourier optics, as discussed in Section 1.1.2. This method is used to compute the wavefront using knowledge of the system and a measured point spread function. There are two primary methods of image-based phase retrieval.

Iterative transform phase retrieval algorithms[9] estimate the phase by repeatedly propagating from the pupil to image planes while maintaining known amplitudes until the model sufficiently matches the measured data. The process of implementing this method is very simple; however, the benefits of the straightforward implementation comes with trade-offs in both accuracy and flexibility [18].

Nonlinear optimization is a more robust, but also more complicated, version of phase retrieval. Nonlinear optimization phase retrieval uses an error metric to construct gradients. The gradients are passed into a minimization function that will adjust the wavefront parameters to minimize the disagreement between the modeled and measured data. This approach offers more flexibility than iterative implementations, and the algorithm is easier to scale for more complicated phase retrieval problems. Additionally, adjustments to the error metric can be used to compensate for real-world effects that are present in the measured data but not in the modeled point spread function[6, 12, 11, 7].

Phase retrieval uses modeled data constructed with the field propagation

technique discussed in Section 1.1.2. The first step in building the forward model is to construct an initial wavefront guess [17] using the known amplitude or pupil function. The initial wavefront is defined using the parameters and a basis set written as

$$W = \sum_n a_n Z_n, \tag{2.1}$$

where a_n is the amplitude of each basis function Z_n. The basis set can be varied depending on the application from a polynomial basis set, like Zernike functions, to a point-by-point wavefront map where each pixel, Z_n has amplitude a_n. The initial wavefront and known amplitude, A, are used to create our pupil function

$$g = A \circ \exp\left(\frac{i2\pi}{\lambda} W\right) \tag{2.2}$$

where $\circ$ represents element-wise multiplication. The pupil function describes the transmission of light through an optical system, and the ability to accurately estimate the phase of a system is dependent on a well-defined pupil function. The "ideal system" with no aberrations and uniform illumination would have a binary mask as a pupil function.

Using field propagation as discussed in section 1.1.2, the Fourier transform is used to propagate the optical field from the pupil plane to the image plane

$$G = \mathrm{FFT}\{g\}. \tag{2.3}$$

The final step in creating modeled data is the intensity calculation

$$I = |G|^2. \tag{2.4}$$

The modeled intensity, or point spread function, is used to define an error metric

$$\epsilon = \frac{\sum_m w_m \circ (\alpha I_m + \beta - D_m)^2}{\sum_m w_m \circ D_m^2} \tag{2.5}$$

where w_m is a weighing function to account for noise and bad pixels in the measured data and D_m is the measured intensity data. α and β are model parameters to account for gain and bias in the measured data which are inherently solved for in the error metric.

There are ways to adjust the forward model depending on the specific problem. For this reason, constructing gradients using algorithmic differentiation offers many advantages. Algorithmic differentiation utilizes a reverse model where the partial derivative of the error metric is propagated in reverse through the individual steps of the forward model. The method is based on algorithmic differentiation discussed in detail in [12]. Propagating through the individual steps creates a more robust and reusable algorithm that eliminates the need to re-derive the gradient calculations when there are modifications to specific steps in the phase retrieval process. For example, during testing one might discover that it is necessary to use a different basis set or error metric. By implementing algorithmic differentiation, these changes can be made without re-deriving the entire error metric gradient.

Below we have the propagation of the gradient through each step in the forward model with the partial derivative denoted by a bar. Starting with the final step in the forward model [12], the error metric yields

$$\bar{I} = 2\alpha w \circ (I - D). \tag{2.6}$$

This propagation using algorithmic differentiation is continued incrementally with

$$\bar{G} = 2G \circ \bar{I}, \tag{2.7}$$

$$\bar{g} = \mathrm{IFFT}\{\bar{G}\}, \tag{2.8}$$

and

$$\bar{W} = \frac{2\pi}{\lambda}\Im[\bar{g} \circ g*] \tag{2.9}$$

until we get to the optimization parameters

$$\bar{a_n} = \sum_m (\bar{W_m} \circ Z_n)_m. \tag{2.10}$$

This provides the gradients necessary to minimize E.

In minimization local minima are often a concern, but, in practice, an accurate optical model should provide sufficient knowledge of the system pupil function to be within the capture range of the algorithm. Focus diversity plays an important role in decreasing the sensitivity to local minima by using multiple point spread functions at different focus positions for phase retrieval. Defocused point spread functions provide more detailed wavefront information that might not be perceivable with a single image and improves the signal to noise ratio of the measured data. This increased sensitivity to wavefront information is particularly important in systems with minimal aberrations.

Focus diversity is introduced into the forward model as

$$g = A \circ e^{\frac{2\pi}{\lambda}(W+W_D)} \tag{2.11}$$

where W_D is a defocused wavefront. For the error metric calculation, the metric is calculated for each diversity image and then added together.

In the conventional case, the well-defined pupil is used to create the forward model, and the difference between the modeled point spread function and the image data is due to the optical aberrations. Optimizing over the parameters used in the forward model to construct the pupil field g produces the solution for the model. This study investigates a case where the pupil function used in the forward model will also represent a source of error in the fitting process.

For this study, I used optical models to generate the measured data, D, and I was able to use a relatively basic implementation of phase retrieval since there was no need to account for real-world artifacts. I generated the forward model using the pupil function for the aligned system. The centered pupil function and a generated point spread function, provided by the modeling software, served as the necessary inputs to the phase retrieval. Throughout this study, I used the centered pupil function while the measured data was created using a decentered pupil function within the modeling software. I optimized over multiple basis sets for the wavefront– specifically tip/tilt, low order Zernike terms, and a point-by-point reconstruction, in that order. This creates a more robust procedure to ensure the accuracy of the point-by-point reconstruction. Additionally, focus diversity was introduced by translating the FPA to five focus positions along the optical axis.

For this application, the goal was to fully understand the effects of pupil knowledge error. There are ways to adjust the phase retrieval recipe to create an algorithm to compensate for these effects. For example, one could optimize with only low order Zernike terms, and the resulting wavefront estimation would disregard the high order noise introduced by the pupil mismatch. In many applications, this could be acceptable, but the final integration testing for a mission of this magnitude requires minimal uncertainty. For this purpose, the goal is not to increase the pupil knowledge error tolerance through algorithm adjustments, but rather to understand how precisely the position of the ground support equipment must be understood before it begins to effect the phase retrieval. In this case, using algorithmic differentiation was necessary because it allowed for minimal algorithm changes as the model evolved throughout the project. The subaperture's effect on the pupil function determined many of the

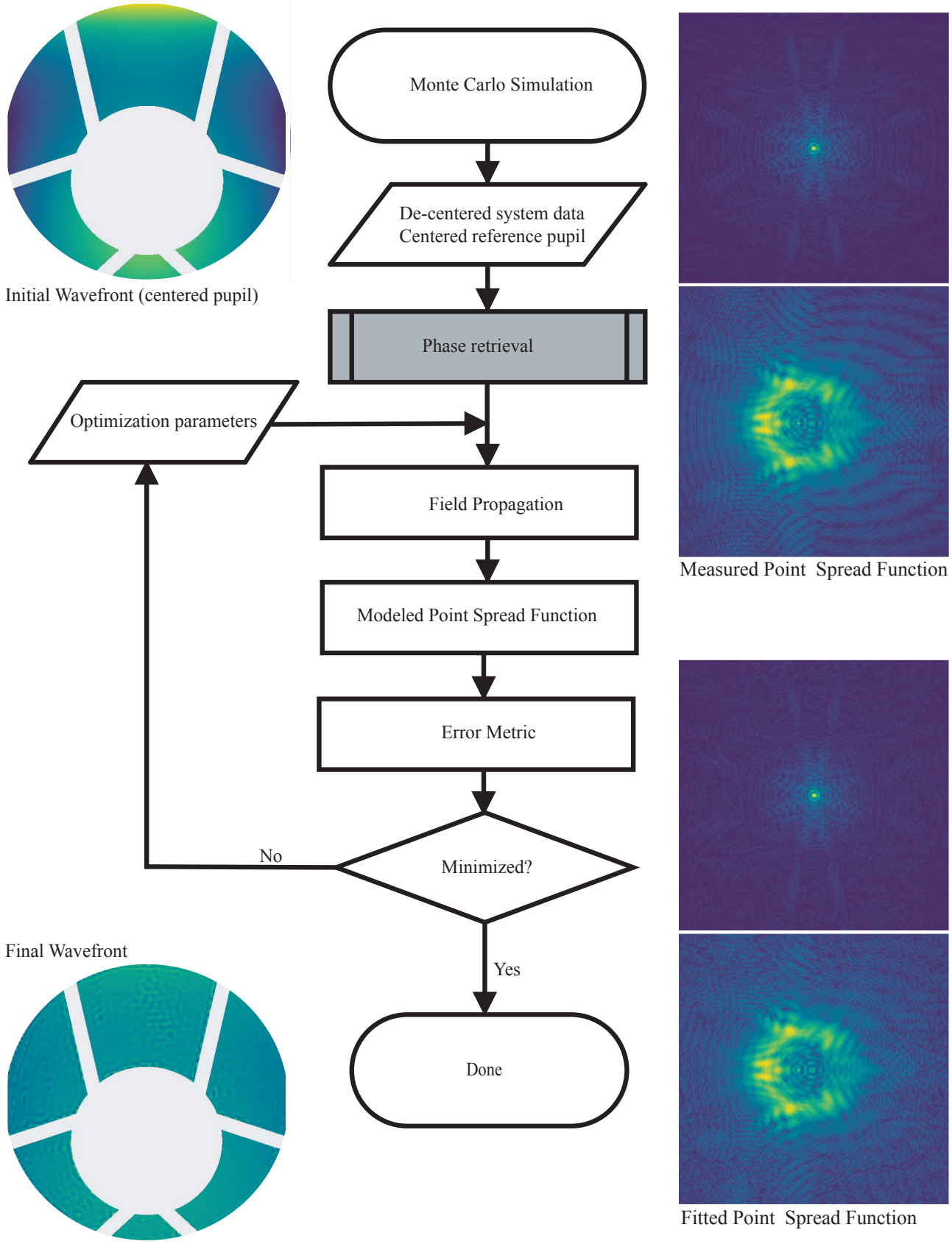


Figure 2.1: Flow diagram of the phase retrieval algorithm using data with a 6 mm decenter of the SAMS

input and model parameters used throughout the study. For example, the sampling relates the size of the image data, pixel size, and pupil sizes to create a sampling ratio, Q, defined by

$$N_p = QN_c \tag{2.12}$$

$$Q = \frac{\lambda f}{D\Delta x} \tag{2.13}$$

for an in-focus system. N_p is the length of the Fourier transform and N_c is the size of the clear aperture in the system pupil in pixels. Additionally, Q can be defined by the wavelength of the system, λ, focal length, f, D the diameter of the clear aperture in physical units, and the pixel size Δx. In this application, the subaperture is an important factor in defining the sampling factor, but since the information is being supplied by the modeling software, it is straightforward to adjust the pupil size and improve the accuracy of the results. Since the subaperture reduces D, a larger pupil size was necessary for the phase retrieval implementation. [11] Without a sufficiently sized pupil function, there were bootstrapping issues in the optimization process that induced higher than expected wavefront error, and the inflexibility of modeling software dictated some of the design choices.

2.2 Simulations

Given that the phase retrieval process involves discrete sampling, we can calculate a general relationship between spatial translation and pixels as

$$\Delta u = \frac{D}{N_p} \tag{2.14}$$

with D being the diameter of the aperture in m and N_p being the number of pixels in the pupil diameter. For example, $\Delta u = \frac{2.4}{1024} = \approx 2.3$ mm. This means

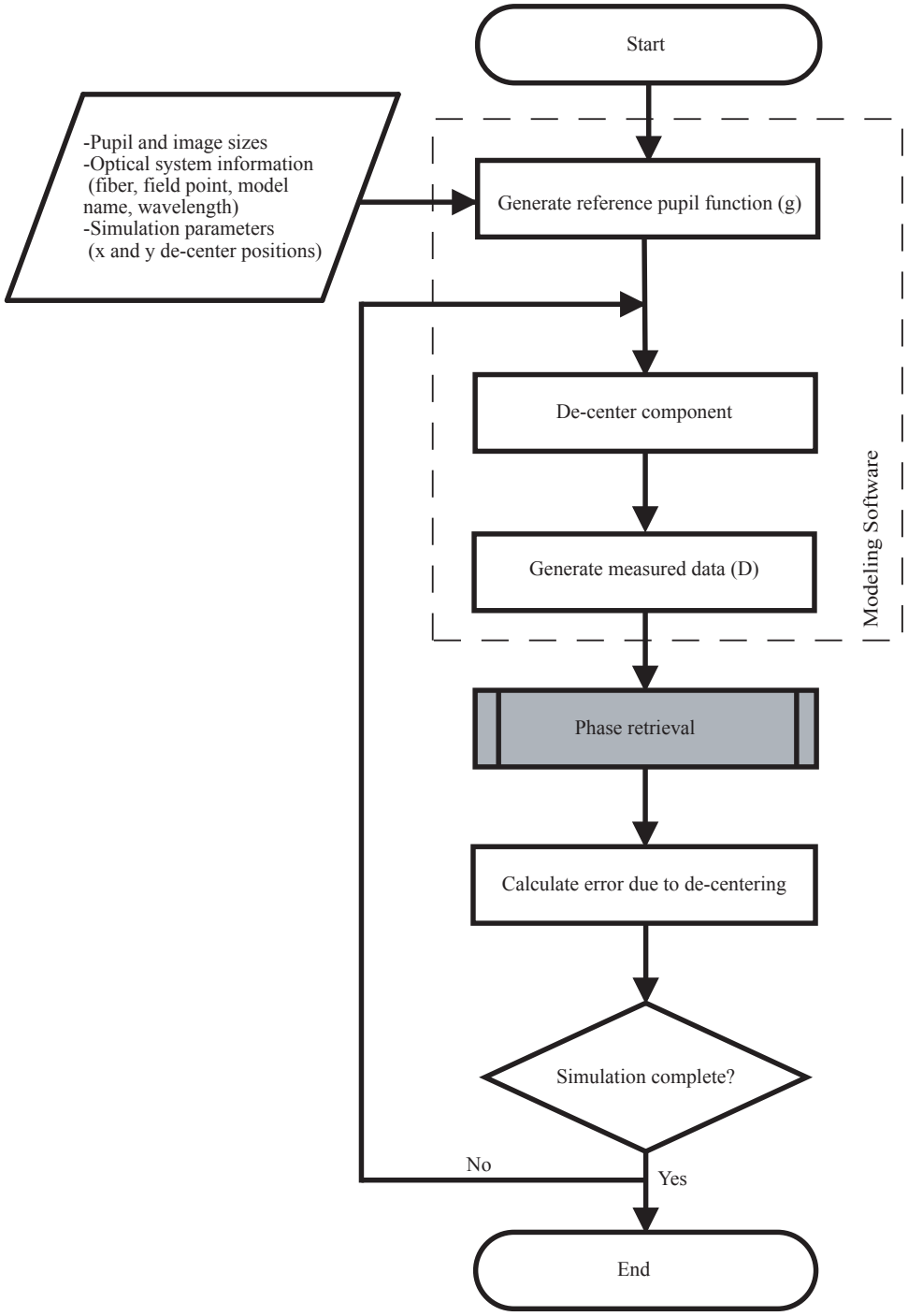


Figure 2.2: Flow diagram for Monte Carlo simulations using modeling software and phase retrieval algorithm

that the pupil could translate by about 2.3 mm before a pixel in the discrete amplitude function changes.

Going beyond the simple calculation of pupil error tolerance, I have conducted a Monte Carlo study to determine how pupil knowledge error affects the phase retrieval beyond the 2.3 mm range. The goal is to define a set radius of allowable decentering for the ground support equipment.

The telescope is modeled in the double-pass configuration along with the ground support equipment. The simulation has many configurations using different fiber sources and field points on the detector to study the pupil knowledge error across the field of view. All of the simulations have focus diversity from FPA translation. The simulation performs phase retrieval using the centered pupil function retrieved from the optical model as the reference pupil. The component is translated in discrete increments, and then the phase retrieval attempts to fit the centered pupil model data to the point spread functions produced by the de-centered system. The purpose of these simulations is to study how phase retrieval behaves with known pupil knowledge error and how that relates to the alignment of the payload to the ground support equipment.

There are three general optical models that will be used in the simulation. The first is an ideal optical model of the pseudo double pass configuration. In this case, the system does not have any perturbed surfaces, or model misalignment. This model provides a baseline of how decentering affects the phase retrieval results in a case where there are no decenter dependent wavefront effects. The pupil geometry varies with fiber and field point location, so each simulation has a unique reference pupil that has different effects on pupil knowledge error. For example, in Figure 1.9 you can see how the positioning of the struts

and secondary mirror vary with the fiber that is being used. The only unknown is the amplitude function; however, the phase retrieval algorithm interprets this ΔA as a difference in wavefront. The outcome of this process provides a general tolerance of decentering that is carried through the subsequent simulations.

The next case is a group of models with simulated misalignment scenarios that are within the alignment tolerances of the instrument. The process of studying the decenter is identical to that for the ideal model, but depending on the perturbation present, the pupil function can respond differently to component decentering. The 30 perturbed models provided insight on how well the simple tolerance, defined using the ideal model, applies to more realistic testing scenarios.

The final model contains gravity sag which introduces significant decenter dependent wavefront changes in addition to the amplitude function mismatch seen in previous models. The gravity sag on the primary mirror introduces significant wavefront effects in the pupil function for the starting wavefront on the order of 8000x compared to the ideal model as show in Figure 2.3. The Root Mean Squared (RMS) WFE in the pupil for an ideal model is approximately 73 nm, but the gravity sag pupil has a RMS WFE of over 8,000 nm. Since the phase retrieval fitting attempts to fill the difference in amplitude function based on the reference pupil, the significant WFE in the gravity sag model will lead to increased decentering effects in the fitting. The combination of the three models will be used to define alignment requirements and expected wavefront error contribution from SAMS decentering.

These three cases have been simulated in a real test configuration where four fibers step across the FPA to sample the entire field of view. The OLAFS was

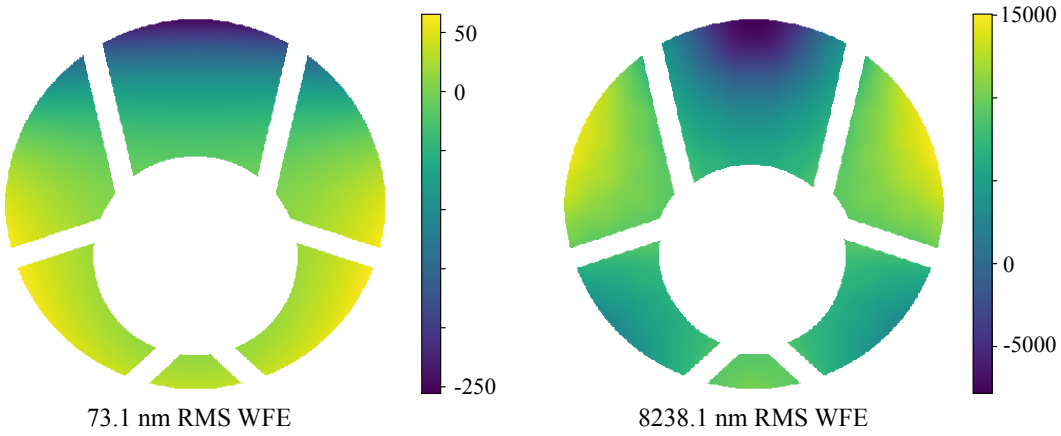


Figure 2.3: A comparison of the reference pupils for the ideal case and gravity sag models showing the significant WFE contribution of the gravity sag on the primary mirror

tilted to six positions to place the four fiber point spread functions on specific field points of the detector[1].

I have visualized the results of this study as a contour map of the WFE where the x and y locations in the plot represent incremental decentering of the SAM-Sin millimeters. This provides a spatial representation of the increased WFE with decentering of the SAMS

CHAPTER 3

RESULTS

3.1 Roman Space Telescope IPA Test Simulations

For a spatial understanding of pupil knowledge error, we show the Δ WFE as a contour plot with respect to the x and y de-centering positions of the SAMS. The ΔW is the RMS WFE of the difference between the initial wavefront, or pupil function, with the wavefront fitted from the phase retrieval. The contour plots visualize the Δ WFE at discrete increments of decentering. Because these are discrete increments, the contour levels only provide a general understanding of decentering effects.

In the optical models there is a centered, imaginary ray that represents a truly double pass configuration with the light originating from and returning to the center of the FPA. I have used this configuration throughout the model simulations as a general comparison in addition to the more realistic test cases.

3.1.1 Ideal Model

The ideal model provided a general understanding for the effects of pupil knowledge error on the phase retrieval algorithm without the effects of the double pass configurations or additional wavefront error in the IPA test configuration. With this model, the results show only the effects of SAMS decentering on the phase retrieval since there are no decentering dependent wavefront effects. This means that the ideal model can be used to understand where the algorithm

is affected by pupil knowledge error. In contrast, the following models confirm that the effects of pupil knowledge error found in the base model, in addition to more realistic model effects, are still within the WFE requirements for the test. To visualize these effects, I have generated a contour plot of the true double pass with the SAMS decentered in 1 mm increments from -7 mm to 7 mm. Within the plot, there are three circles with defined radii. Based on this plot, I concluded that the effect of pupil knowledge error on the phase retrieval results becomes more apparent with decentering greater than 4 mm in any direction.

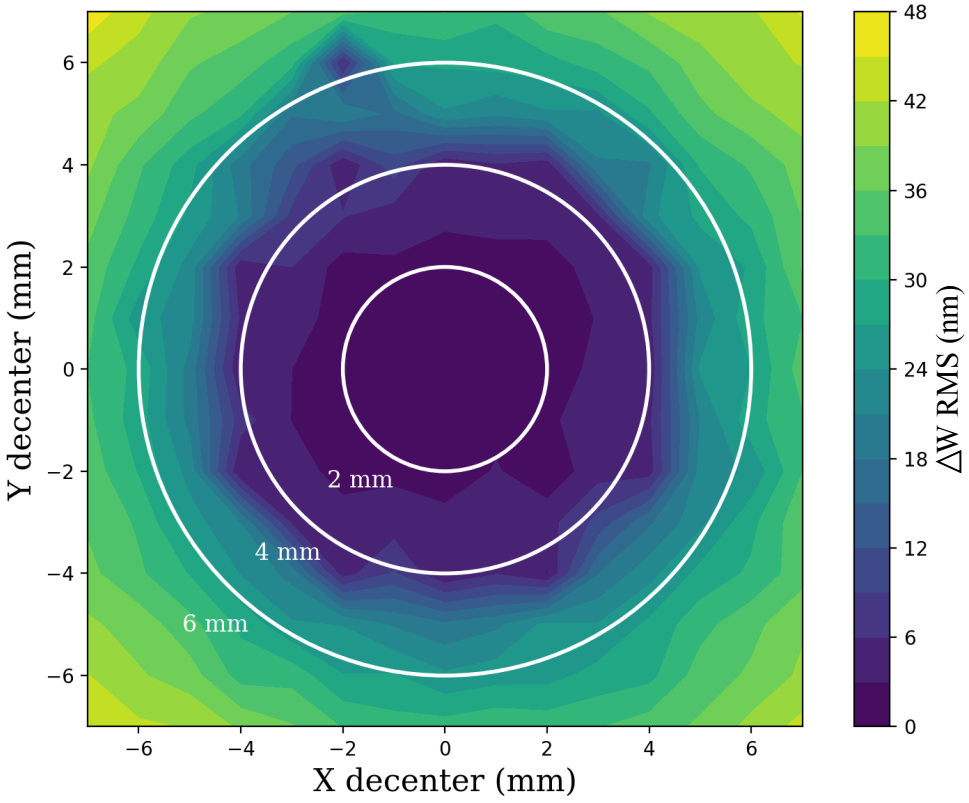


Figure 3.1: A study of SAMS decentering from -7 mm to 7 mm in 1 mm increments visualized as a contour plot for the ideal model

The FPA has 18 detectors and four fibers adjacent to the detector on either side– represented visually in Figure 3.4. I started by looking at the effects of fiber location. To show that the results are consistent across multiple fibers, I

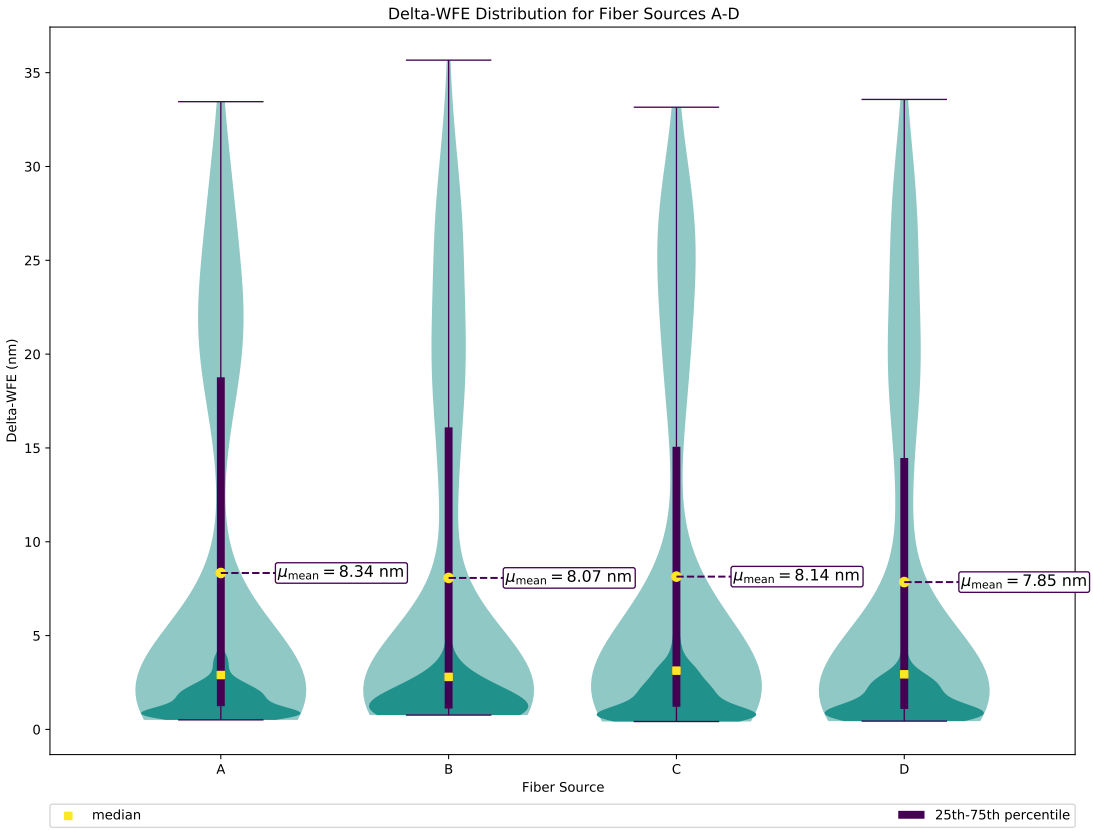


Figure 3.2: Violin plot of Δ WFE across fibers A-D at a center field point with the lighter violin and box plot showing the results of -6 mm to 6 mm decenter with 1 mm step sizes, and the darker violin contour showing the distribution of Δ WFE values within a 4 mm decentering radius

have the violin plot in Figure 3.2 of the ΔW of fibers A-D, on the left side of the FPA, with an overlay of the mean, median, and 1st and 3rd quartiles. The ΔW within the 4 mm is shown as a darker violin plot. Based on the shape of the violin, this plot shows that the fours fiber positions have consistent ΔWFE effects from pupil knowledge error. Additionally, it confirms the initial findings that the 4 mm radius of decentering shows significantly less ΔWFE.

Using the 4 mm radius as an initial requirement, I ran the decentering study for a full test sweep across the FPA as shown in Figure 1.8. The full test sweep involves illuminating four fibers at once and translating them across the FPA

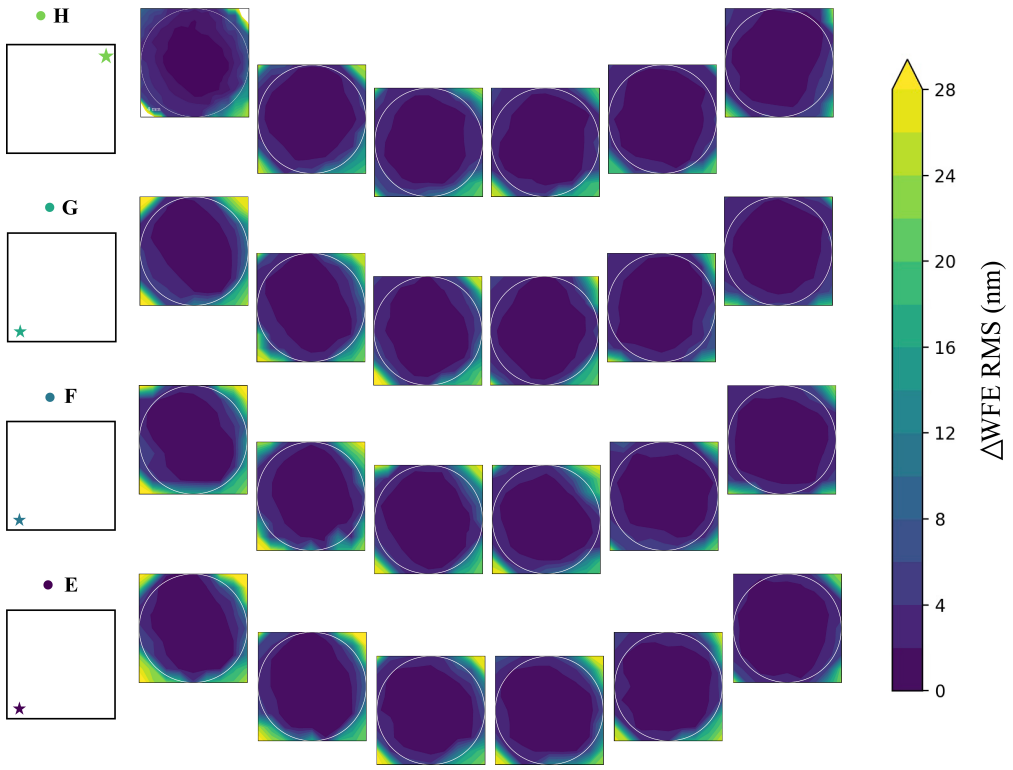


Figure 3.3: The contour plots of each fiber and field point pair across the field of view the example test pass shown in 3.3 with the 4 mm radius overlayed

with six OLAFS tilt positions. In this case, the fibers are aimed in the lower left-hand corner, represented by stars, with the fiber detector pairs indicated by the color. The contour plots shown represent the individual contours from each fiber on the detectors with the top rows having results from fiber G and H. The contour plots shown have set contour levels with a maximum of 25 RMS Δ WFE, and the 4 mm radius is overlayed for comparison. As seen in Figure 3.3, all field points across the FPA show minimal effects of SAMS decentering on the phase retrieval within the 4 mm radius. This is further demonstrated with Figure 3.4 which shows the 95th percentile and maximum ΔW for each of the contour plots shown in 3.3. All field points had a 95th percentile ΔW of less than 6 nm. By observing the pupil functions for these fiber-field point pairs, it shows that the test cases with more complex pupil geometry generally

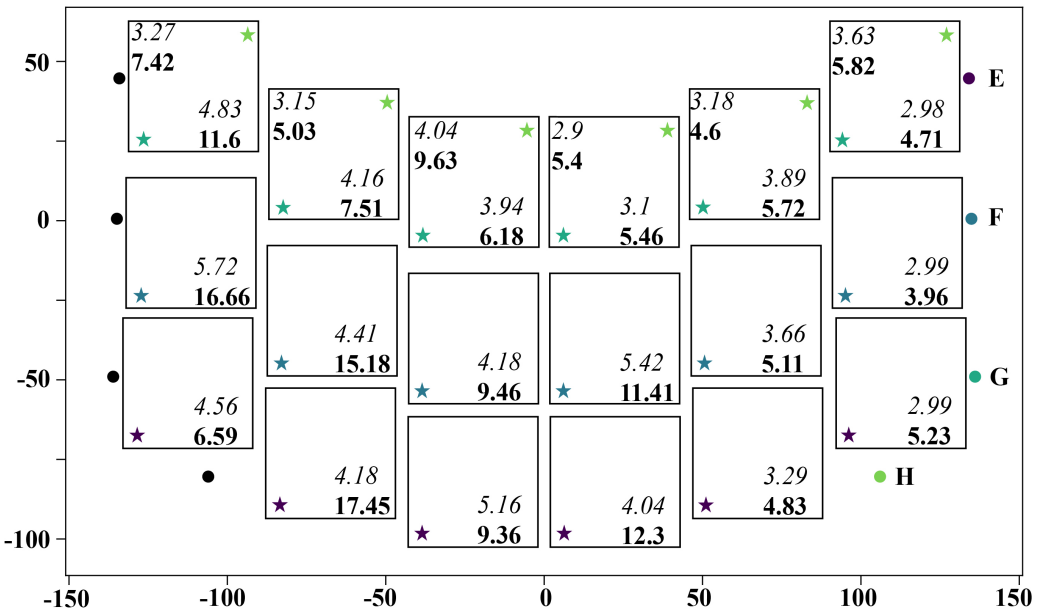


Figure 3.4: A diagram for the results of the ideal model showing the 95th percentile Δ WFE and maximum Δ WFE for the field points illuminated by fibers E-H throughout the test pass

increased the effects of pupil knowledge error– especially in test cases with a double strut created by the angle of the light leaving and returning through the telescope. This is demonstrated in Figure 3.9. The ideal model did not have the clipping discussed in the following section, but the complex pupil geometry is consistent in all models.

3.1.2 Monte Carlo Perturbed Models

Moving on from the ideal case, I used 30 perturbed models with realistic misalignment scenarios within tolerance for the telescope. The purpose of this set of models is to ensure that the initial 4 mm radius of decentering is consistent throughout configurations that may be encountered during the test. These models have random variations, and the goal was to verify that there were not any

significant deviations from the results of the ideal model.

These results are visualized in Figure 3.5 which shows the box plots for each of the 30 models. The top plot has the simulation results decentering from -6 mm to 6 mm, and the lower plot shows the results within the 4 mm radius. The results are consistent with the ideal model with the largest 95th percentile ΔW being less than 8 nm. These plots also provide a visual reference of how significant the decentering effect becomes along the steep edges outside of the 4 mm radius seen in the contour representation.

The consistency throughout the 30 models indicated that no further investigation was necessary for characterizing the effects of misalignments within tolerance. This means that there was not a reason to carry these perturbed surfaces throughout the following studies with gravity sag.

3.1.3 Gravity Sag Model

During IPA testing, gravity can not be offloaded, which results in deformation of the primary mirror and introduces significant wavefront error. The effect of gravity sag increases the initial WFE as shown in Figure 2.3 and causes increased ΔW from the decenter dependent wavefront effects in the pupil function. While analyzing these simulations, I maintained the 4 mm decentering tolerance and set contour levels from the previous model results. First I used the imaginary, true double pass simulation result plotted with the same decentering step size and range as the ideal model. There was a significant increase in ΔW due to the pupil function with significant RMS WFE from gravity sag. This trend was seen across the entire field of view. At this point in my analysis, I noticed an

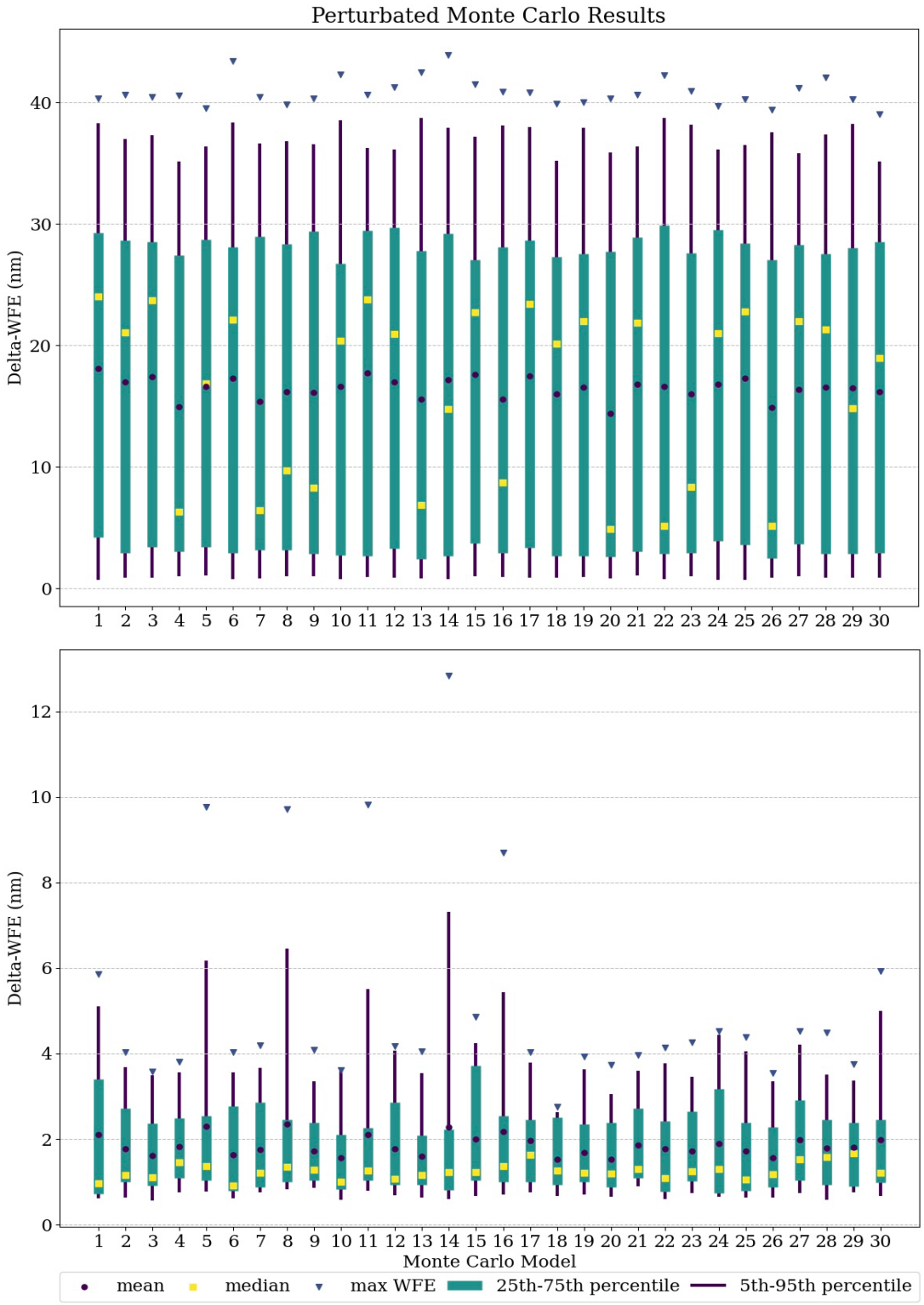


Figure 3.5: The results of the 30 perturbed models as box plots with a 6 mm radius and 4 mm radius of decentering

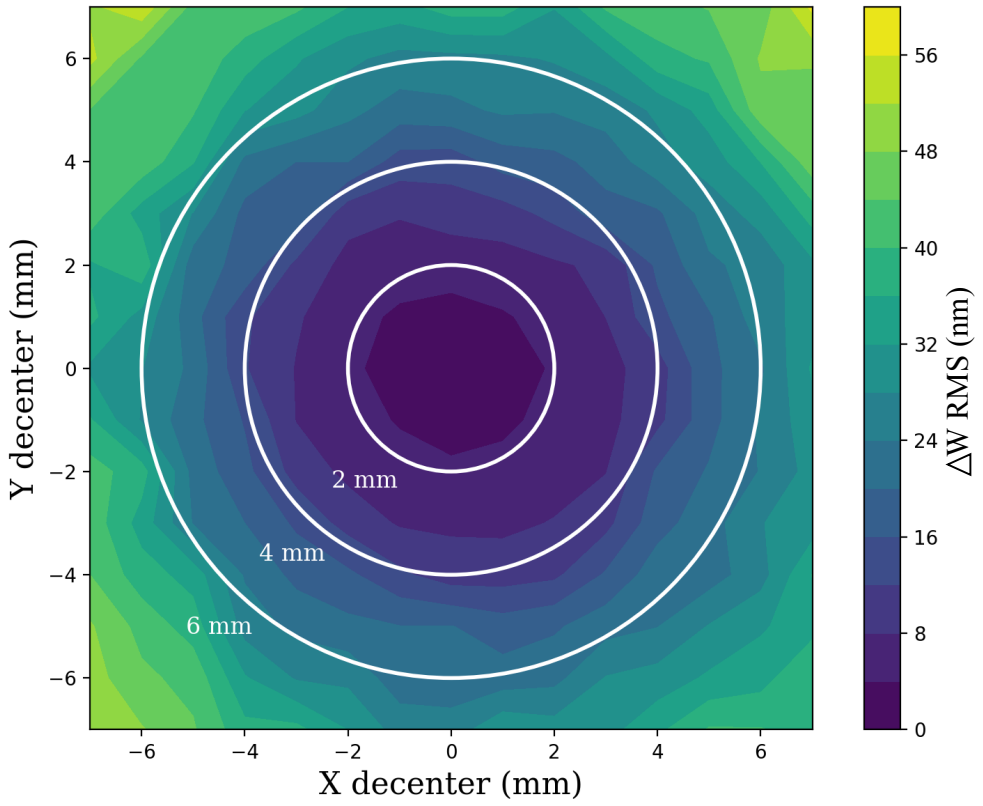


Figure 3.6: A study of SAMS decentering from -7 mm to 7 mm in 1 mm increments visualized as a contour plot for the gravity sag model

inconsistency in the data at certain field points, and upon investigation, found that the pupil function from the model had unexplained clipping along the top edge of the aperture as shown in Figure 3.9. Currently, there is no straightforward solution to this issue, and it has been determined that there is most likely an issue with the modeling software itself as opposed to this particular model. This clipping introduced additional WFE, but since the goal is to determine if the worst case WFE is compatible with the WFE budget, I am able to use this analysis for the conclusions. The clipping was not present at every field point shown in Figure 3.7, so I have used this in combination with the numerical results to compare the effect that the clipping has on the WFE. The increased clipping on the left side of the FPA corresponds to higher WFE. Based on Figure

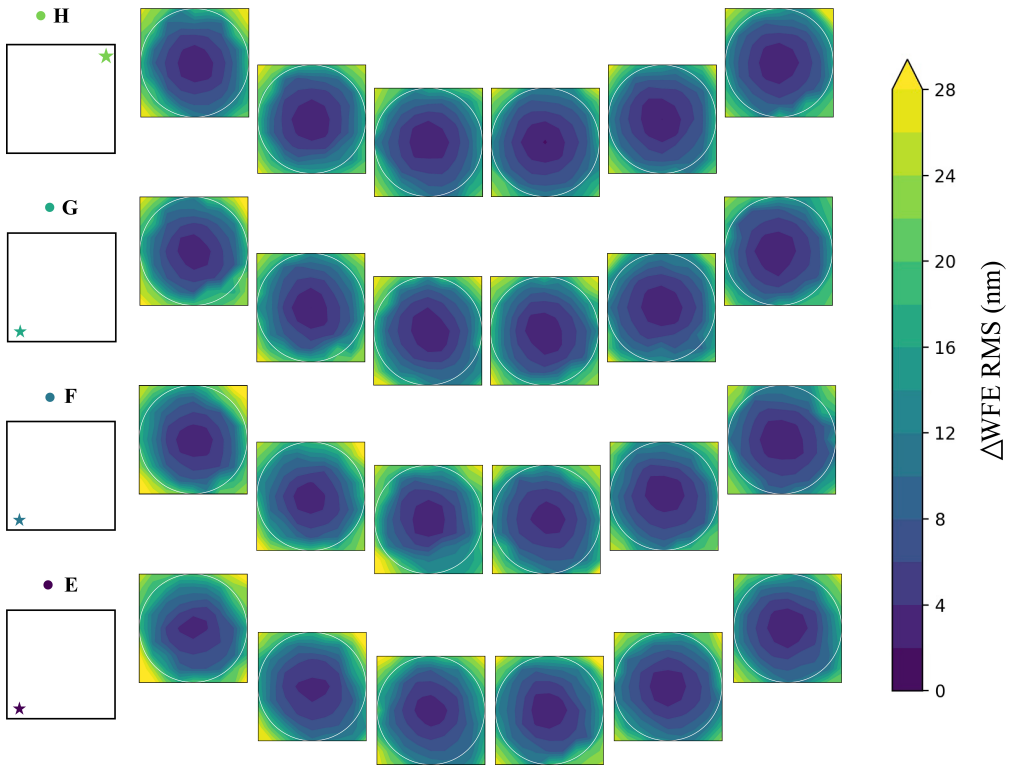


Figure 3.7: The contour plots of each fiber and field point pair across the field of view the example test pass shown in 3.7 with the 4 mm radius overlayed for the gravity sag model

3.8, the clipping effects are more pronounced than the influence of the complex pupil geometries that we saw in the ideal model case.

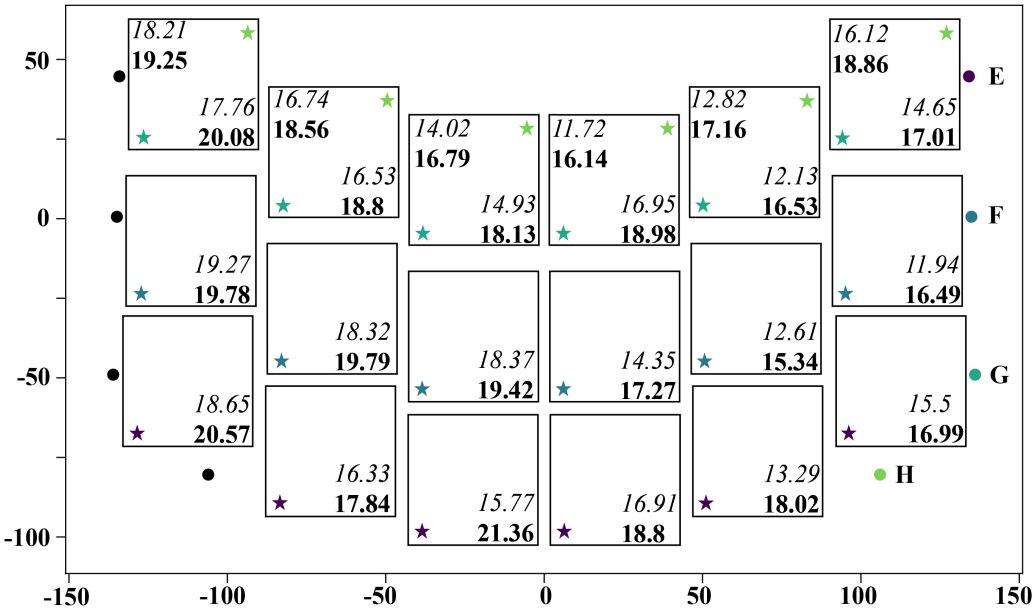


Figure 3.8: A diagram for the results of the gravity sag model showing the 95th percentile ΔW and maximum Δ WFE for fiber locations and field points of the test pass

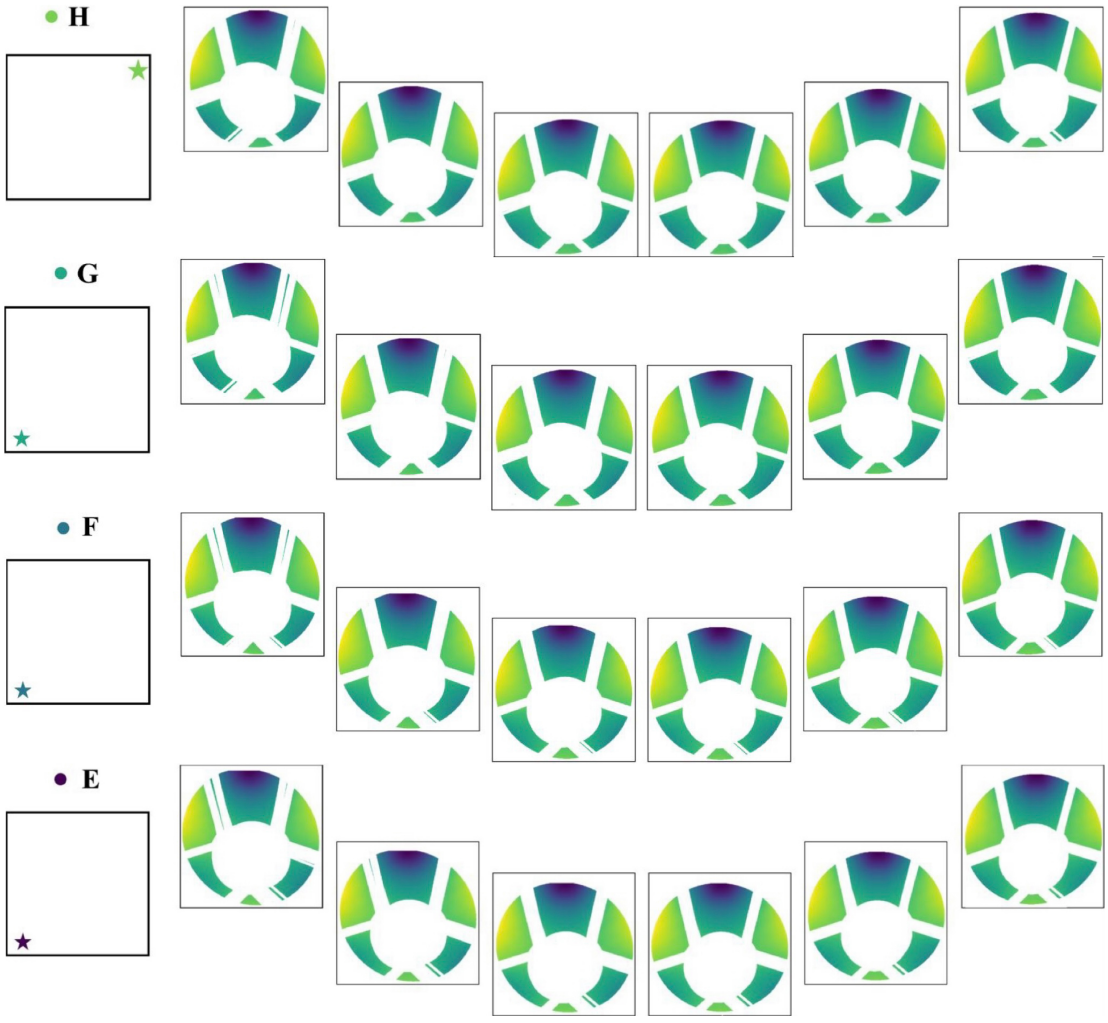


Figure 3.9: Pupil clipping of fibers E-H as beams are translated across FPA

CHAPTER 4
CONCLUSION

The goal of this study was to determine how pupil knowledge error affects phase retrieval–specifically for the IPA testing of the Roman Space Telescope. With the initial study, I determined that the effect of decentering on the phase retrieval algorithm alone was minimal within a 4 mm radius of decentering. These results showed how the algorithm performs without additional WFE sources. The subsequent studies verified that the addition of decenter-dependent WFE in the perturbed and gravity sag results WFE were within the range of the allocated WFE budgeted for this aspect of the test.

I established that the phase retrieval algorithm could tolerate 4mm decentering in each direction without a significant contribution to WFE. This result showed the effectiveness of the algorithm in handling the pupil knowledge error. Applying this finding to multiple field points and fiber locations strengthened this conclusion. I then analyzed the effects with 30 perturbed models with randomized surface effects that model more realistic telescope configurations. Even in the presence of the random effects, I saw no indication that the 4 mm tolerance should be modified to account for these perturbations. The results from these models reinforced my original findings from the ideal model. Given this conclusion, I studied the gravity sag models with the intentions of determining how much WFE could be expected in the real test. At this point in the study, I intended to define the limit at 4 mm unless results from the gravity sag model were too significant to fit with the WFE budget for this aspect of the testing. The gravity sag model results, even with the added WFE contribution and pupil clipping artifact, fit within the WFE requirements, and I concluded

that the pupil knowledge error induced by SAMS misalignment within a 4 mm range was acceptable for the IPA testing of RST.

BIBLIOGRAPHY

[1] Matthew D. Bergkoetter and Alden S. Jurling. Data analysis algorithm for double-pass testing of the Roman Space Telescope. In José Sasián and Richard N. Youngworth, editors, *Optical System Alignment, Tolerancing, and Verification XIII*, volume 11488, pages 167 – 173. International Society for Optics and Photonics, SPIE, 2020.

[2] Matthew R. Bolcar. The Roman Space Telescope optical system: overview, test, and verification. In Laura E. Coyle, Shuji Matsuura, and Marshall D. Perrin, editors, *Space Telescopes and Instrumentation 2022: Optical, Infrared, and Millimeter Wave*, volume 12180, page 121801M. International Society for Optics and Photonics, SPIE, 2022.

[3] NASA Goddard Space Flight Center. Observatory- technical.

[4] NASA Goddard Space Flight Center. Roman space telescope mission overview.

[5] Bruce H. Dean, David L. Aronstein, J. Scott Smith, Ron Shiri, and D. Scott Acton. Phase retrieval algorithm for JWST Flight and Testbed Telescope. In John C. Mather, Howard A. MacEwen, and Mattheus W. M. de Graauw, editors, *Space Telescopes and Instrumentation I: Optical, Infrared, and Millimeter*, volume 6265, page 626511. International Society for Optics and Photonics, SPIE, 2006.

[6] J. R. Fienup. Phase retrieval algorithms: a comparison. *Appl. Opt.*, 21(15):2758–2769, Aug 1982.

[7] J. R. Fienup. Phase-retrieval algorithms for a complicated optical system. *Appl. Opt.*, 32(10):1737–1746, Apr 1993.

[8] J. R. Fienup, J. C. Marron, T. J. Schulz, and J. H. Seldin. Hubble space telescope characterized by using phase-retrieval algorithms. *Appl. Opt.*, 32(10):1747–1767, Apr 1993.

[9] R. W. Gerchberg. A practical algorithm for the determination of phase from image and diffraction plane pictures. *Optik*, 35:237–246, 1972.

[10] Joseph M. Howard, Kuo-Chia (Alice) Liu, Michael Akkerman, Martina I. Atanassova, Carl Blaurock, Kong Ha, Gregory Michels, and Carson McDonald. Integrated modeling activities for NASA's Roman Space Tele-

scope. In George Z. Angeli and Philippe Dierickx, editors, *Modeling, Systems Engineering, and Project Management for Astronomy X*, volume 12187, page 121870V. International Society for Optics and Photonics, SPIE, 2022.

[11] Alden S. Jurling, Matthew D. Bergkoetter, and James R. Fienup. Techniques for arbitrary sampling in two-dimensional fourier transforms. *J. Opt. Soc. Am. A*, 35(11):1784–1796, Nov 2018.

[12] Alden S. Jurling and James R. Fienup. Applications of algorithmic differentiation to phase retrieval algorithms. *J. Opt. Soc. Am. A*, 31(7):1348–1359, Jul 2014.

[13] Goodman J.W. *Introduction to Fourier Optics*. Electrical Engineering Series. McGraw-Hill, 1996.

[14] Nasa. The hubble space telescope optical systems failure report. 1990.

[15] Jane Rigby, Marshall Perrin, Michael McElwain, Randy Kimble, Scott Friedman, Matt Lallo, René Doyon, Lee Feinberg, Pierre Ferruit, Alistair Glasse, Marcia Rieke, George Rieke, Gillian Wright, Chris Willott, Knicole Colon, Stefanie Milam, Susan Neff, Christopher Stark, Jeff Valenti, Jim Abell, Faith Abney, Yasin Abul-Huda, D. Scott Acton, Evan Adams, David Adler, Jonathan Aguilar, Nasif Ahmed, Loïc Albert, Stacey Alberts, David Aldridge, Marsha Allen, Martin Altenburg, Javier Alvarez Marquez, Catarina Alves de Oliveira, Greg Andersen, Harry Anderson, Sara Anderson, Ioannis Argyriou, Amber Armstrong, Santiago Arribas, Etienne Artigau, Amanda Arvai, Charles Atkinson, Gregory Bacon, Thomas Bair, Kimberly Banks, Jaclyn Barrientes, Bruce Barringer, Peter Bartosik, William Bast, Pierre Baudoz, Thomas Beatty, Katie Bechtold, Tracy Beck, Eddie Bergeron, Matthew Bergkoetter, Rachana Bhatawdekar, Stephan Birkmann, Ronald Blazek, Claire Blome, Anthony Boccaletti, Torsten Boeker, John Boia, Nina Bonaventura, Nicholas Bond, Kari Bosley, Ray Boucarut, Matthew Bourque, Jeroen Bouwman, Gary Bower, Charles Bowers, Martha Boyer, Larry Bradley, Greg Brady, Hannah Braun, David Breda, Pamela Bresnahan, Stacey Bright, Christopher Britt, Asa Bromenschenkel, Brian Brooks, Keira Brooks, Bob Brown, Matthew Brown, Patricia Brown, Andy Bunker, Matthew Burger, Howard Bushouse, Steven Cale, Alex Cameron, Peter Cameron, Alicia Canipe, James Caplinger, Francis Caputo, Mihai Cara, Larkin Carey, Stefano Carniani, Maria Carrasquilla, Margaret Carruthers, Michael Case, Riggs Catherine, Don Chance, George Chapman, Stéphane Charlot, Brian Charlow, Pierre Chayer, Bin Chen, Brian Cherinka, Sarah Chichester, Zack Chilton, Taylor Chonis, Mark Clampin, Charles Clark, Kerry Clark, Dan Coe, Benee Coleman, Brian Comber, Tom Comeau,

Dennis Connolly, James Cooper, Rachel Cooper, Eric Coppock, Matteo Correnti, Christophe Cossou, Alain Coulais, Laura Coyle, Misty Cracraft, Mirko Curti, Steven Cuturic, Katherine Davis, Michael Davis, Bruce Dean, Amy DeLisa, Wim deMeester, Nadia Dencheva, Nadezhda Dencheva, Joseph DePasquale, Jeremy Deschenes, Örs Hunor Detre, Rosa Diaz, Dan Dicken, Audrey DiFelice, Matthew Dillman, William Dixon, Jesse Doggett, Tom Donaldson, Rob Douglas, Kimberly DuPrie, Jean Dupuis, John Durning, Nilufar Easmin, Weston Eck, Chinwe Edeani, Eiichi Egami, Ralf Ehrenwinkler, Jonathan Eisenhamer, Michael Eisenhower, Michelle Elie, James Elliott, Kyle Elliott, Tracy Ellis, Michael Engesser, Nestor Espinoza, Odessa Etienne, Mireya Etxaluze, Patrick Falini, Matthew Feeney, Malcolm Ferry, Joseph Filippazzo, Brian Fincham, Mees Fix, Nicolas Flagey, Michael Florian, Jim Flynn, Erin Fontanella, Terrance Ford, Peter Forshay, Ori Fox, David Franz, Henry Fu, Alexander Fullerton, Sergey Galkin, Anthony Galyer, Macarena Garcia Marin, Jonathan Gardner, Lisa Gardner, Dennis Garland, Bruce Garrett, Danny Gasman, Andras Gaspar, Daniel Gaudreau, Peter Gauthier, Vincent Geers, Paul Geithner, Mario Gennaro, Giovanna Giardino, Julien Girard, Mark Giuliano, Kirk Glassmire, Adrian Glauser, Stuart Glazer, John Godfrey, David Golimowski, David Gollnitz, Fan Gong, Shireen Gonzaga, Michael Gordon, Karl Gordon, Paul Goudfrooij, Thomas Greene, Matthew Greenhouse, Stefano Grimaldi, Andrew Groebner, Timothy Grundy, Pierre Guillard, Irvin Gutman, Kong Q. Ha, Peter Haderlein, Andria Hagedorn, Kevin Hainline, Craig Haley, Maryam Hami, Forrest Hamilton, Heidi Hammel, Carl Hansen, Tom Harkins, Michael Harr, Jessica Hart, Quyen Hart, George Hartig, Ryan Hashimoto, Sujee Haskins, William Hathaway, Keith Havey, Brian Hayden, Karen Hecht, Chris Heller-Boyer, Caroline Henriques, Alaina Henry, Karl Hermann, Scarlin Hernandez, Brigette Hesman, Brian Hicks, Bryan Hilbert, Dean Hines, Melissa Hoffman, Sherie Holfeltz, Bryan J. Holler, Jennifer Hoppa, Kyle Hott, Joseph Howard, Rick Howard, Alexander Hunter, David Hunter, Brendan Hurst, Bernd Husemann, Leah Hustak, Luminita Ilinca Ignat, Garth Illingworth, Sandra Irish, Wallace Jackson, Amir Jahromi, Peter Jakobsen, LeAndrea James, Bryan James, William Januszewski, Ann Jenkins, Hussein Jirdeh, Phillip Johnson, Timothy Johnson, Vicki Jones, Ron Jones, Danny Jones, Olivia Jones, Ian Jordan, Margaret Jordan, Sarah Jurczyk, Alden Jurling, Catherine Kaleida, Phillip Kalmanson, Jens Kammerer, Huijo Kang, Shaw-Hong Kao, Diane Karakla, Patrick Kavanagh, Doug Kelly, Sarah Kendrew, Herbert Kennedy, Deborah Kenny, Ritva Keski-kuha, Charles Keyes, Richard Kidwell, Wayne Kinzel, Jeff Kirk, Mark Kirkpatrick, Danielle Kirshenblat, Pamela Klaassen, Bryan Knapp, J. Scott Knight, Perry Knollenberg, Robert Koehler, Anton Koekemoer, Aiden Kovacs, Trey Kulp, Nimisha Kumari, Mark Kyprianou, Stephanie La Massa, Aurora Labador, Alvaro Labiano Ortega, Pierre-Olivier Lagage, Charles-Phillipe Lajoie, Matthew Lallo, May Lam, Tracy

Lamb, Scott Lambros, Richard Lampenfield, James Langston, Kirsten Larson, David Law, Jon Lawrence, David Lee, Jarron Leisenring, Kelly Lepo, Michael Leveille, Nancy Levenson, Marie Levine, Zena Levy, Dan Lewis, Hannah Lewis, Mattia Libralato, Paul Lightsey, Miranda Link, Lily Liu, Amy Lo, Alexandra Lockwood, Ryan Logue, Chris Long, Douglas Long, Charles Loomis, Marcos Lopez-Caniego, Jose Lorenzo Alvarez, Jennifer Love-Pruitt, Adrian Lucy, Nora Luetzgendorf, Peiman Maghami, Roberto Maiolino, Melissa Major, Sunita Malla, Eliot Malumuth, Elena Manjavacas, Crystal Mannfolk, Amanda Marrione, Anthony Marston, André Martel, Marc Maschmann, Gregory Masci, Michaela Masciarelli, Michael Maszkiewicz, John Mather, Kenny McKenzie, Brian McLean, Matthew McMaster, Katie Melbourne, Marcio Meléndez, Michael Menzel, Kaiya Merz, Michele Meyett, Luis Meza, Cherie Miskey, Karl Misselt, Christopher Moller, Jane Morrison, Ernie Morse, Harvey Moseley, Gary Mosier, Matt Mountain, Julio Mueckay, Michael Mueller, Susan Mullally, Jess Murphy, Katherine Murray, Claire Murray, David Mustelier, James Muzerolle, Matthew Mycroft, Richard Myers, Kaila Myrick, Shashvat Nanavati, Elizabeth Nance, Omnarayani Nayak, Bret Naylor, Edmund Nelan, Bryony Nickson, Alethea Nielson, Maria Nieto-Santisteban, Nikolay Nikolov, Alberto Noriega-Crespo, Brian O'Shaughnessy, Brian O'Sullivan, William Ochs, Patrick Ogle, Brenda Oleszczuk, Joseph Olmsted, Shannon Osborne, Richard Ottens, Beverly Owens, Camilla Pacifici, Alyssa Pagan, James Page, Sang Park, Keith Parrish, Polychronis Patapis, Lee Paul, Tyler Pauly, Cheryl Pavlovsky, Andrew Pedder, Matthew Peek, Maria Pena-Guerrero, Konstantin Pennanen, Yesenia Perez, Michele Perna, Beth Perriello, Kevin Phillips, Martin Pietraszkiewicz, Jean-Paul Pinaud, Norbert Pirzkal, Joseph Pitman, Aidan Piwowar, Vera Platais, Danielle Player, Rachel Plesha, Joe Pollizi, Ethan Polster, Klaus Pontoppidan, Blair Porterfield, Charles Proffitt, Laurent Pueyo, Christine Pulliam, Brian Quirt, Irma Quispe Neira, Rafael Ramos Alarcon, Leah Ramsay, Greg Rapp, Robert Rapp, Bernard Rauscher, Swara Ravindranath, Timothy Rawle, Michael Regan, Timothy A. Reichard, Carl Reis, Michael E. Ressler, Armin Rest, Paul Reynolds, Timothy Rhue, Karen Richon, Emily Rickman, Michael Ridgaway, Christine Ritchie, Hans-Walter Rix, Massimo Robberto, Gregory Robinson, Michael Robinson, Orion Robinson, Frank Rock, David Rodriguez, Bruno Rodriguez Del Pino, Thomas Roellig, Scott Rohrbach, Anthony Roman, Fred Romelfanger, Perry Rose, Anthony Roteliuk, Marc Roth, Braden Rothwell, Neil Rowlands, Arpita Roy, Pierre Royer, Patricia Royle, Chunlei Rui, Peter Rumler, Joel Runnels, Melissa Russ, Zafar Rustamkulov, Grant Ryden, Holly Ryer, Modhumita Sabata, Derek Sabatke, Elena Sabbi, Bridget Samuelson, Benjamin Sapp, Bradley Sappington, B. Sargent, Arne Sauer, Silvia Scheithauer, Everett Schlawin, Joseph Schlitz, Tyler Schmitz, Analyn Schneider, Jürgen Schreiber, Vonessa Schulze, Ryan Schwab, John Scott, Kenneth Sembach, Clare Shanahan, Bryan Shaughnessy, Richard Shaw,

Nanci Shawger, Christopher Shay, Evan Sheehan, Sharon Shen, Allan Sherman, Bernard Shiao, Hsin-Yi Shih, Irene Shivaei, Matthew Sienkiewicz, David Sing, Marco Sirianni, Anand Sivaramakrishnan, Joy Skipper, Gregory Sloan, Christine Slocum, Steven Slowinski, Erin Smith, Eric Smith, Denise Smith, Corbett Smith, Gregory Snyder, Warren Soh, Tony Sohn, Christian Soto, Richard Spencer, Scott Stallcup, John Stansberry, Carl Starr, Elysia Starr, Alphonso Stewart, Massimo Stiavelli, Amber Straughn, David Strickland, Jeff Stys, Francis Summers, Fengwu Sun, Ben Sunnquist, Daryl Swade, Michael Swam, Robert Swaters, Robby Swoish, Joanna M. Taylor, Rolanda Taylor, Maurice Te Plate, Mason Tea, Kelly Teague, Randal Telfer, Tea Temim, Deepashri Thatte, Christopher Thompson, Linda Thompson, Shaun Thomson, Tuomo Tikkanen, William Tippet, Connor Todd, Sharon Toolan, Hien Tran, Edwin Trejo, Justin Truong, Chris Tsukamoto, Samuel Tustain, Harrison Tyra, Leonardo Ubeda, Kelli Underwood, Michael Uzzo, Julie Van Campen, Thomas Vandal, Bart Vandenbussche, Begoña Vila, Kevin Volk, Glenn Wahlgren, Mark Waldman, Chanda Walker, Michel Wander, Christine Warfield, Gerald Warner, Matthew Wasiak, Mitchell Watkins, Andrew Weaver, Mark Weilert, Nick Weiser, Ben Weiss, Sarah Weissman, Alan Welty, Garrett West, Lauren Wheate, Elizabeth Wheatley, Thomas Wheeler, Rick White, Kevin Whiteaker, Paul Whitehouse, Jennifer Whiteleather, William Whitman, Christina Williams, Christopher Willmer, Scott Willoughby, Andrew Wilson, Gregory Wirth, Emily Wislowski, Erin Wolf, David Wolfe, Schuyler Wolff, Bill Workman, Ray Wright, Carl Wu, Rai Wu, Kristen Wymer, Kayla Yates, Christopher Yeager, Jared Yeates, Ethan Yerger, Jinmi Yoon, Alice Young, Susan Yu, Dean Zak, Peter Zeidler, Julia Zhou, Thomas Zielinski, Cristian Zincke, and Stephanie Zonak. Characterization of JWST science performance from commissioning. *arXiv e-prints*, page arXiv:2207.05632, July 2022.

[16] Koby Z. Smith, D. Scott Acton, Laura E. Coyle, Taylor S. Chonis, Ben Gallagher, and J. Scott Knight. Methodology and results of james webb space telescope thermal vacuum optical system alignment testing and analysis. *34th Space Symposium*, 2018.

[17] Samuel T. Thurman. Method of obtaining wavefront slope data from through-focus point spread function measurements. *Journal of the Optical Society of America. A, Optics, image science, and vision*, 28 1:1–7, 2011.

[18] Samuel T. Thurman and James R. Fienup. Phase retrieval with signal bias. *J. Opt. Soc. Am. A*, 26(4):1008–1014, Apr 2009.